PRECIPITATION OF OXIDE DISPERSION STRENGTH STEELS AFTER LONG-TERM ANNEALING AT TEMPERATURE OF 475 °C

Dávid Košovský[a,*], Marcel Miglierini[a,b], Tomáš Kmječ[c,d],
Július Dekan[a], Marek Bujdoš[e]

[a] *Slovak University of Technology in Bratislava, Faculty of Electrical Engineering and Information Technology, Institute of Nuclear and Physical Engineering, Ilkovičova 3, 841 04 Bratislava, Slovakia*

[b] *Czech Technical University in Prague, Faculty of Nuclear Science and Physical Engineering, Department of Nuclear Reactors, V Holešovičkách 2, 180 00 Praha, Czech Republic*

[c] *Charles University, Faculty of Mathematics and Physics, V Holešovičkách 2, 180 00 Praha, Czech Republic*

[d] *Czech Academy of Sciences, Institute of Physics, Na Slovance 2, 182 00 Praha, Czech Republic*

[e] *Comenius University, Faculty of Natural Sciences, Ilkovičova 6, 842 15 Bratislava, Slovakia*

[*] corresponding author: david.kosovsky@stuba.sk

ABSTRACT. Oxide dispersion strengthened steels are key alloys used in nuclear installations. Steels with chromium content of up to 10 wt % are suitable due to their advantageous properties and these alloys are used for the construction of technological devices in the primary circuit of nuclear power plants. From other studies, it can be concluded that chromium has anti-corrosive properties due to the formation of a passivation layer, which results in reduced activation of the material by thermal neutrons. Macroscopic properties are determined by their microstructure, and therefore, the description of the microstructure is important. Transmission Mössbauer spectroscopy and atom probe tomography were used to characterise the material. This provides information about the physical and/or chemical environment of the resonant atoms can be obtained. Obtained spectral parameters reach saturation values from which the solubility limit of chromium in iron can be determined. In Cr-rich phase, the solubility limit can be estimated from the value of spectral parameters of the single-line in the spectrum annealed for the longest time. The suggested procedures are subsequently applied to the case studies of stainless steels suitable for the construction of various components of the III+/IVth generation of nuclear reactors (including fast and fusion reactors).

KEYWORDS: High-chromium steel, hyperfine interactions, Mössbauer spectrometry, atom probe tomography, stainless steel, ferritic-martensitic steel.

1. INTRODUCTION

Technological progress in the nuclear industry is largely determined by the development of construction materials. Different types of alloys are suitable for advanced applications, and therefore, it is necessary to analyse them using different experimental nuclear-physical techniques [1–9]. Undoubtedly, the most important alloys used in the primary circuit are anti-corrosion steels, where, in addition to carbon, other elements, such as chromium, manganese, nickel, and titanium, are added to improve their physical, chemical, and mechanical properties [10–21].

Development of ferritic-martensitic oxide dispersion strengthened (ODS) steels was paralleled by material research for fast reactors with the reduced swelling under higher neutron fluxes. The main advantage of ODS steels is their low neutron activation even at high neutron fluxes (up to $10^{14}\,\mathrm{m^{-2}s^{-1}}$) [22, 23]. Along with the appearance of fusion reactor material programmes, ODS steels also became attractive for the use as base materials in the design of nuclear fusion facilities. A block and sub-block martensite microstructure is responsible for the high strength and toughness

of ODS steels as well as increased resistance to volumetric swelling under neutron irradiation [24, 25]. The closest application of the ODS steels in nuclear fusion environment is the structural material for the test blanket module for the tritium breeding in fusion reactors. However, the sharp increase in the ductile-to-brittle transition temperature of the steels is one of the undesirable characteristics of their use in a fusion environment. When the irradiation temperature is below 350 °C, the formation of dislocation loops, precipitates of α'-phase, and solute-rich clusters leads to dislocation pinning, thus, suppressing the plastic deformation, which is determined by particle distribution in a material [26, 27]. ODS steels consist of iron-base matrix with oxide particles dispersed in it. They have high heat resistance, strength, and ductility. Alloys of nickel, chromium, and manganese are the most common ones, but this class of materials also includes iron-aluminium alloys [28–30].

Oxide dispersion strengthening is based on incoherency of the oxide particles within the lattice of the material. Coherent particles have a continuous lattice plane from the matrix to the particle, whereas incoher-

ent particles do not have this continuity, and therefore, both lattice planes terminate at the interface. This mismatch in interfaces results in a high interfacial energy which inhibits dislocation [31, 32]. On the other hand, the oxide particles are stable in the matrix, which prevents creep. Particle stability implies little dimensional change, embrittlement, effects on properties, stable particle spacing, and general resistance to modifications at high temperatures [33, 34].

Precipitation of α' (Cr-rich) phase causes significant embrittlement of the alloy, which leads to changes in other mechanical properties with the highest embrittlement rate at 475 °C. The local chromium content in α'-phase is higher than 80 at %, which causes local embrittlement of the steel. Conversely, the σ-phase is prone to precipitation if the annealing temperature is between 490 °C and 830 °C and the chromium concentration is between 15 at % and 85 at %. The phase decomposition of the α' precipitations at a temperature of 475 °C results in the formation of α (Fe-rich) and α' (Cr-rich) phases. The applicability of Mössbauer spectrometry is suitable for the characterisation of phases in high-chromium steels, due to different magnetic properties at a room temperature (RT). Specifically, α (Fe-rich) phase has ferromagnetic properties at RT and α' (Cr-rich) phase exhibits paramagnetic properties [35–42].

For the analysis of the microstructure of metallic materials, there are many nuclear-physical techniques that provide information not only from the surface of the material, but also from the material's bulk. Steels containing carbon and further additive elements, such as Cr, Mn, Ni, and Ti, belong, without doubt, among the most important alloys used as construction materials of the primary circuit of nuclear power plants. Transmission Mössbauer spectroscopy (TMS) is one of the most sensitive methods, because it is characterised by unprecedented energetic resolution of the order of neV. Using the measured spectra, we can determine the valence state of the atoms, electrical field gradient, hyperfine magnetic field at the location of the resonating nuclei created by their electron shells, and electron fields of the nearby ions. From the areas of the individual spectral magnetic and paramagnetic components, we can describe the arrangement of cations in the material structure, and from the relative intensities of sextet lines, the orientation of the local magnetic moments [35, 36].

In this work, we studied the microstructure of ODS steel PM80KhV2, which excels in mechanical resistance, corrosion resistance, and high hardness due to the presence of chromium carbides and Y_2O_3 clusters. PM80KhV2 steel with nominal chromium concentration of 20 wt % is suitable for applications where the chemical resistance of the surface is crucial. High chromium content increases toughness, hardness, and tensile strength. Chromium oxides are segregated in surface, thereby contributing to the formation of passivation layers. Sulphur contributes to the machin-

ability of the material, but in higher concentrations it is considered as an impurity and can contribute to unwanted pitting corrosion. Most materials from the category of very hard steels have significantly reduced toughness. Steel PM80KhV2 is an exception and has a toughness comparable to ordinary steels even at 61 hrc (according to the Rockwell hardness test). The conventional hardening temperature is 990–1120 °C for 20 minutes. Subsequently, the steel material is tempered, where the selected temperature is directly proportional to the resulting hardness, for example, a tempering temperature of 150 °C results in hardness of 61 hrc, while a tempering temperature of 660 °C results only in 54 hrc.

It is a common practise to combine Mössbauer spectroscopy investigations with other experimental methods to acquire more complex information about the studied materials. In our research, we have used X-Ray Fluorescence (XRF) and Atom Probe Tomography (APT). The XRF is based on primary excitation of atoms in the sample by high-energy X-ray radiation and subsequent de-excitation of atoms via characteristic radiation. The APT was used for three-dimensional description of Cr-rich precipitates. Atom probe tomography is a nanoscale analysis technique that provides three-dimensional spatial imaging with high sensitivity. The technique relies on ionisation and subsequent field evaporation of individual atoms or atomic clusters from a studied sample (around 0.1–0.35 nm resolution in depth and 0.35–0.52 nm laterally) [43–45].

In this work, we discuss the possibility of using theoretical procedures applicable to Mössbauer data, which have so far only been used in the evaluation of model binary Fe-Cr alloys. The aim of this article is to demonstrate the use of different evaluation approaches to derive Mössbauer spectral parameters from real materials with special emphasis on high-chromium ODS steels PM80KhV2, which have a significant application potential in nuclear industry. Using a theoretical fitting model, it is possible to directly quantify the probabilities of the occurrence of individual elements in the immediate vicinity of the resonant ^{57}Fe nuclei using several magnetic components. Values of spectral parameters saturate, and therefore, the Avrami's precipitation mechanism can be used to describe microstructural changes during thermal annealing at a temperature of 475 °C.

2. Materials and methods

The samples of ODS steels studied in this work are referred to as high-chromium steels because the concentration of chromium is higher than 10 wt %. Metallic materials in powder form enriched with yttrium oxide particles (Y_2O_3) with a purity between 99 % and 99.5 % were used as precursors for the production of PM80KhV2 steel samples. The particles were consolidated by hot isostatic pressing (HIP). Subsequently, the ferritic structure recrystallised at the

value of 0.9 of the melting temperature. After solidification at a rate of $\dot{T} = 10.4\,°C\,s^{-1}$, the steel plates were cold rolled, then heat-treated at a temperature of 1137 °C for 80 minutes, followed by rapid cooling to 717 °C. The resulting steel samples were formed into 3 (±0.2) mm thick plates.

To simulate the effect of thermal embrittlement at a temperature of 475 °C, the PM80KhV2 samples were annealed in a high-temperature furnace in medium vacuum (0.54 Pa) for 1012 hours. For the transmission Mössbauer spectroscopy measurements, the material was removed from different areas of the plate samples using a titanium drill covered with a diamond coating at low speeds so as not to chemically or thermally degrade the powdered samples. The samples were drilled to a deep depth, so the powdered material is mainly from the bulk and not just from the surface.

Qualitative XRF analysis was carried out using the Amptek Experimenter's XRF Kit, which contains an X-ray tube (Mini-X) and a high-resolution X-ray detector with signal processing electronics (X-123). The X-ray Wolfram tube was operated at 40 kV with the current of 15 µA. As a detector, a Si-PIN diode was used (size 6 mm², silicon thickness 500 µm, 12.5 µm thick beryllium window, energy resolution 145 eV FWHM @ 5.9 keV). They were performed with the sample surface positioned at 45° with respect to the X-ray beam direction and 45° to the detector (in one layer). Data analysis was performed using ADMCA software.

Exact chemical composition was checked by Flame Atomic Absorption Spectroscopy (F-AAS) using spectrometer Perkin Elmer 1100.

Finally, the chemical composition was determined using Optical Emission Spectroscopy (OES) High-End spark spectrometer SPECTROLAB S, which has a high sensitivity even for light elements in steels. The measurement took place in an argon atmosphere with the help of UV-C radiation (120–240 nm) using a CMOS + T semiconductor detector. The ultrastable spark (with a frequency of 1000 Hz) is provided by means of a plasma generator. Before measurement, the calibration was performed using low-alloy steel 100Cr6.

The TMS measurements were performed at RT using a conventional Wissel TMS spectrometer working in constant acceleration mode and equipped with a ^{57}Co/Rh radiation source. The calibration of the velocity scale was performed by an α-Fe foil; the isomer shift values are given relative to the centre of its TMS spectrum recorded at RT. The spectra were analysed using the least squares method assuming Lorentzian line shapes and deconvolution using the Confit program [46]. In the evaluation process, spectral parameters of the individual sextets comprising their relative area (A_{rel}), line width (Γ), average hyperfine magnetic field ($\langle B_{hf} \rangle$), average isomer shift ($\langle IS \rangle$), and χ^2- parameter were refined during the fit. Quadrupole shifts were not considered. In order to decrease the overall number of the refined parameters, relative line intensities of 1:A21:1/3 of the corresponding line pairs in the sextets were assumed. The parameter A21 was fitted only for one, the so-called determining sextet, which has the highest probability. Line intensities of the remaining sextets were coupled to those of the determining one and fixed during the evaluation.

APT analyses were performed using the EIKOS-UV atom probe microscope which provides three-dimensional tomography with nanoscale characterisation of microstructures and high spatial resolution single atom detection with high efficiency. IVAS (CAMECA) software was used for data reconstruction. The APT technique is particularly suitable if the impurity concentration is well above the miscibility limit (gap) and provides information of the time evolution of the phase composition (and decomposition), size, and morphology of the analysed precipitates.

The Energy Compressed Tomographic Atom Probe (ECTAP) mode was used for the measurements of all samples and the experimental instrument was equipped with an aDLD detector. The presence of the Energy Compressed Lens (ECL) provides high quality resolution of the mass spectrum and the aDLD detector minimises losses due to the element or event overlap during the multi-event detection. The experimental conditions were set in such a way that it was possible to determine the phase distribution in the sample as accurately as possible and to minimise the preferential evaporation of chromium. In ECTAP measurements, it is actually necessary to isolate the precipitates in the material, for which a data filter is used, since the nominal chromium concentration in the matrix is between 5 and 60 at %. Therefore, a threshold of 60 at % was chosen to prevent the contribution of chromium atoms from the homogeneous matrix. This value is subsequently calculated around each atom in a spherical volume with a radius of 0.5 nm. The determined composition and morphology is therefore determined with an accuracy of ±1 at % and ±1 nm.

3. RESULTS AND DISCUSSION

3.1. CHEMICAL ANALYSIS

The qualitative analysis of ODS steel samples was performed by XRF. The measured spectrum of PM80KhV2 steel compared with spectrum of binary $Fe_{100-x}Cr_x$ ($x = 22.1$ at %) alloy is shown in Figure 1. The spectrum clearly shows that the studied steel contains mostly iron and chromium, and the representation of other elements is negligible. The determined chemical composition of PM80KhV2 steel samples measured using F-AAS and OES is shown in Table 1.

3.2. TRANSMISSION MÖSSBAUER SPECTROSCOPY

In order to evaluate the TMS spectra of ODS PM80KhV2 steel samples, a model based on Gaussian
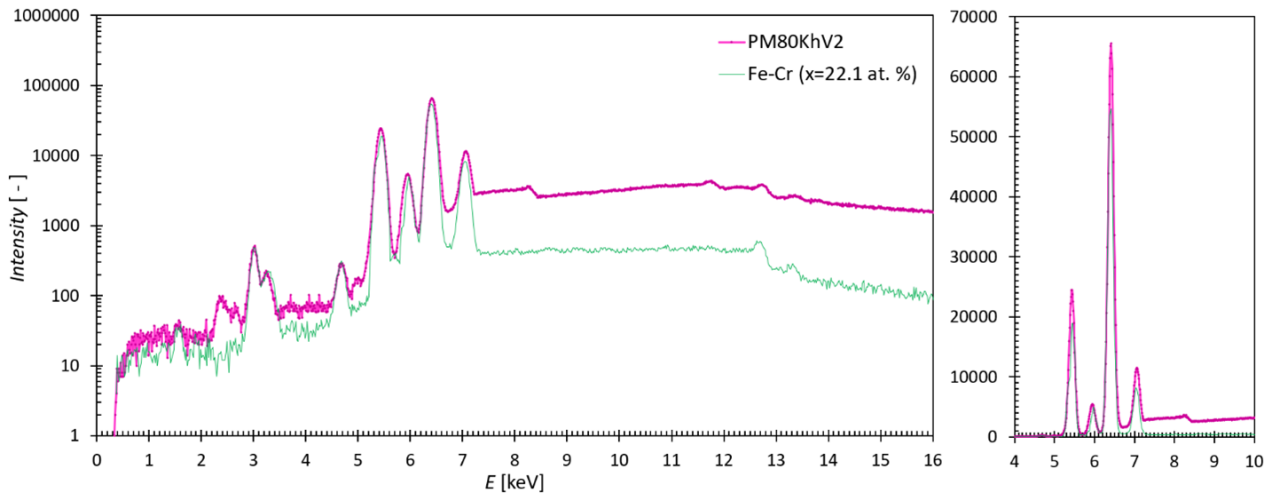
FIGURE 1. XRF spectrum of the PM80KhV2 steel compared with that of binary $Fe_{100-x}Cr_x$ ($x = 22.1\,at\,\%$).

Technique/element	Concentration [wt %]									
	Fe	C	Cr	Mn	P	Si	S	V	Mo	Ni
Nominal	79.50	0.20	20.10	0.59	<0.01	0.40	<0.01	0.04	-	0.10
F-AAS	78.90	-	19.50	-	-	-	-	-	-	0.10
OES	79.40	0.22	20.50	0.56	<0.01	0.32	<0.01	0.04	0.04	0.13

TABLE 1. Chemical composition of samples of steel PM80KhV2 determined by F-AAS and OES.

distribution function was used. This model is suitable for alloys where the concentration of alloying elements is more than 15 at % [42, 47].

Because the analysed samples predominantly consist of chromium and iron, we have applied a distribution function model for binary alloys to describe the dominant (>98 %) part of the crystallographic components. Its broad spectral lines (sextets) were refined by convolutions of a narrow Lorentzian sextet with a Gaussian distribution [41].

Gaussian distribution model (GDM) consists of three distributed sextets with the intensity ratio of the first to the third lines (A31) fixed at 0.333 and the Lorentzian sextet linewidth fixed at $0.25\,mm\,s^{-1}$. We assume a bcc character of the binary alloy model; therefore, the quadrupole shifts are set to zero. The minor paramagnetic feature in the middle of the spectra was described by a single Lorentzian line whose linewidth, isomer shift, and relative area were refined.

The first and the second distributed sextets correspond to iron atoms located in the first nearest neighbour (1NN), and in the second nearest neighbour (2NN), respectively. The third sextet (with the smallest relative area) represents a contribution of the atoms outside the 1NN and the 2NN of the resonant nuclei. In the centre of the spectrum, a paramagnetic component was indicated, a singlet associated with Cr-rich precipitates [48–59].

The measured spectra of the non-annealed sample and the sample annealed for 1012 hours fitted with the GDM model are shown in Figure 2.

The individual magnetic components exhibit hyper-fine magnetic fields of approximately 29.2 T, 25.1 T, and 19.5 T (Figure 3). The average hyperfine magnetic field derived from the three distributed sextets moderately increases with annealing time and saturates at about 26.8(5) T as shown in Figure 4. Variations in the average hyperfine magnetic field can be related to re-arrangement of non-ferrous nuclides in the vicinity of the resonant atoms. Tiny modifications of the isomer shift with the annealing time are within the error range. Thus, possible changes in the chemical composition of the steel as a result of annealing can be ruled out. Rather, a re-arrangement of the constituent elements can be considered.

The values of the hyperfine magnetic fields saturate with annealing time, from which the formation of the chromium rich α' phase can be deduced. Variations in the average hyperfine magnetic field can be related to changes in the presence-arrangement of non-ferrous nuclides in the vicinity of the resonant atoms, reflecting the local arrangement of the alloy change during annealing. It has been demonstrated in article by Dubiel et al. [42] for binary alloy that the kinetics of the annealing induced processes could be well described in terms of the Johnson-Mehl-Avrami-Kolmogorov (JMAK) equation. The JMAK model is used to describe the crystallisation kinetics in different materials including ODS steels. It assumes that the crystallisation is isothermal (nucleation and growth occur at constant temperature). Additional conditions are that the sample is infinitely large, and nucleation is random throughout the sample volume, grain growth is isotropic until the crystals collide, and the activation
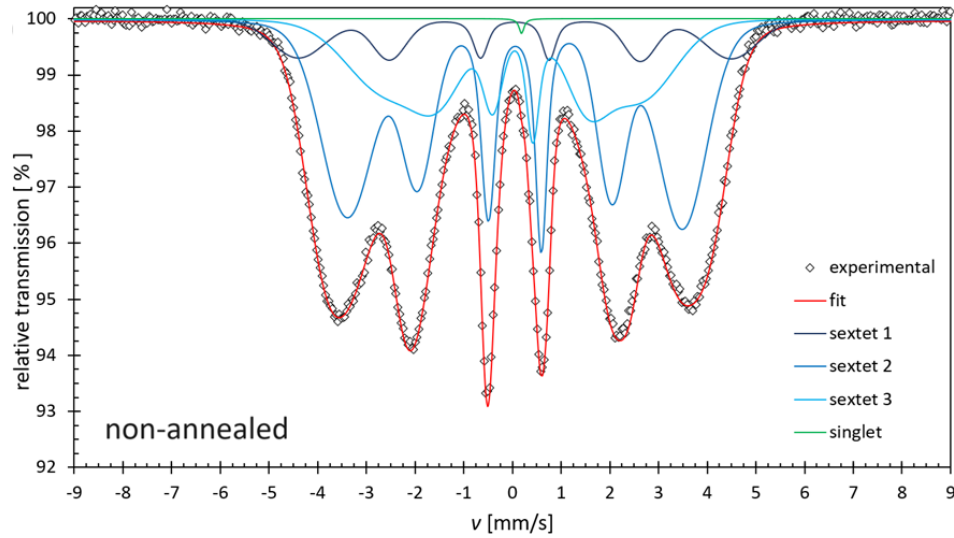
(A). As-received (non-annealed) state.
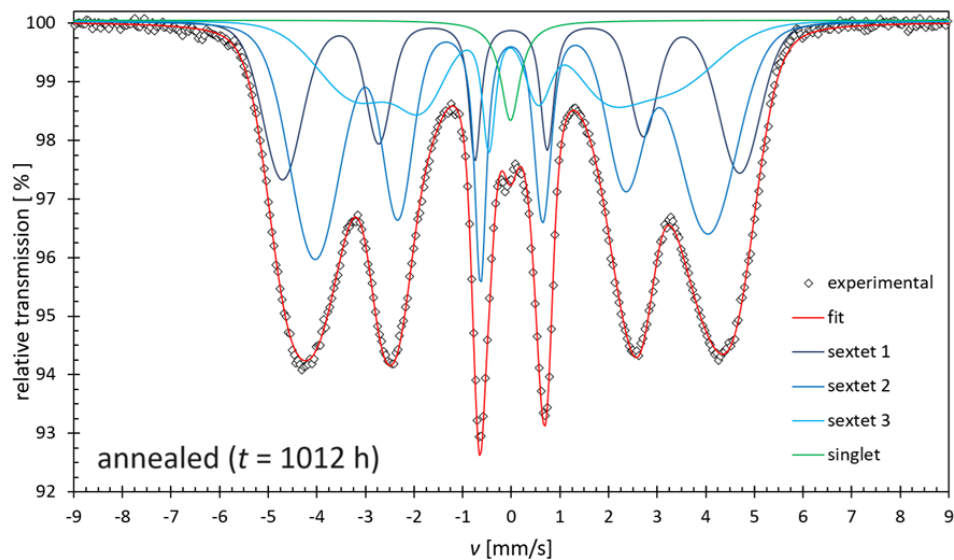
(B). After 1012 hours of annealing at 475 °C.

FIGURE 2. Fitted transmission Mössbauer spectra of PM80KhV2 ODS steel measured at RT in as-received (non-annealed) state, and after 1012 hours of annealing at 475 °C.
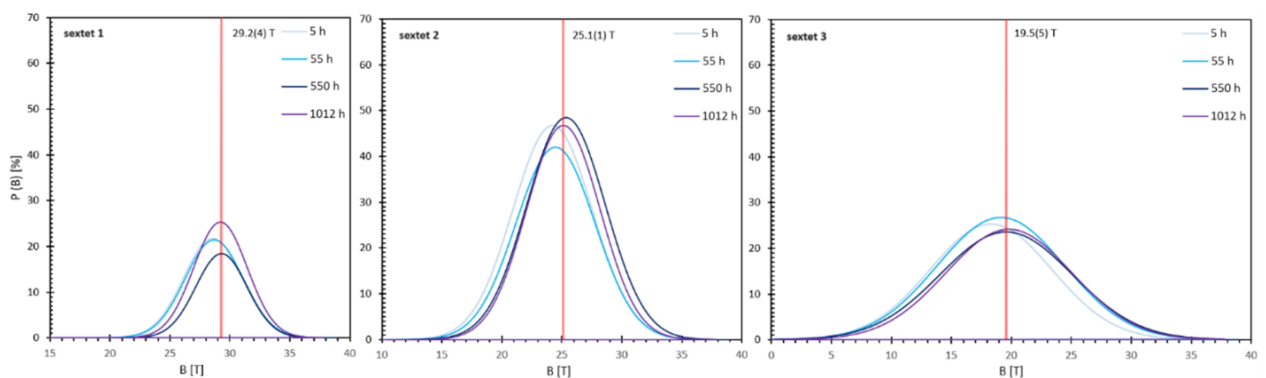

FIGURE 3. Comparison between the magnetic hyperfine field distribution P(B)-curves derived from the TMS spectra annealed for different annealing times between 0 and 1012 hours.
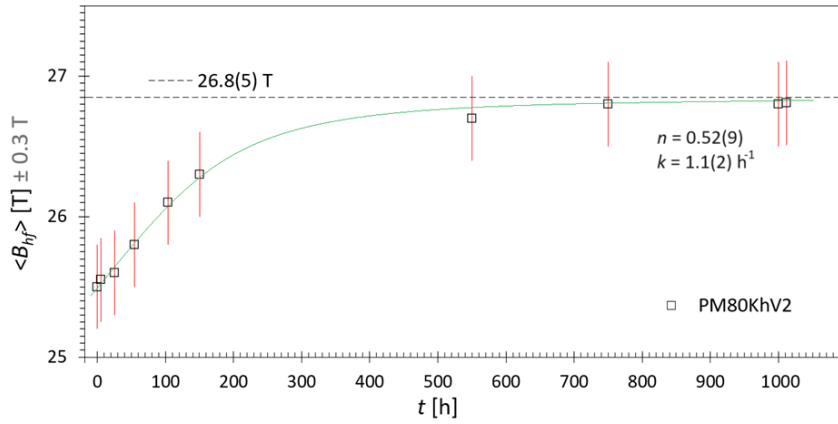
Figure 4. Dependence of the average magnetic hyperfine field on the annealing time for the PM80KhV2 steel sample annealed at a temperature of 475 °C measured by TMS at RT.
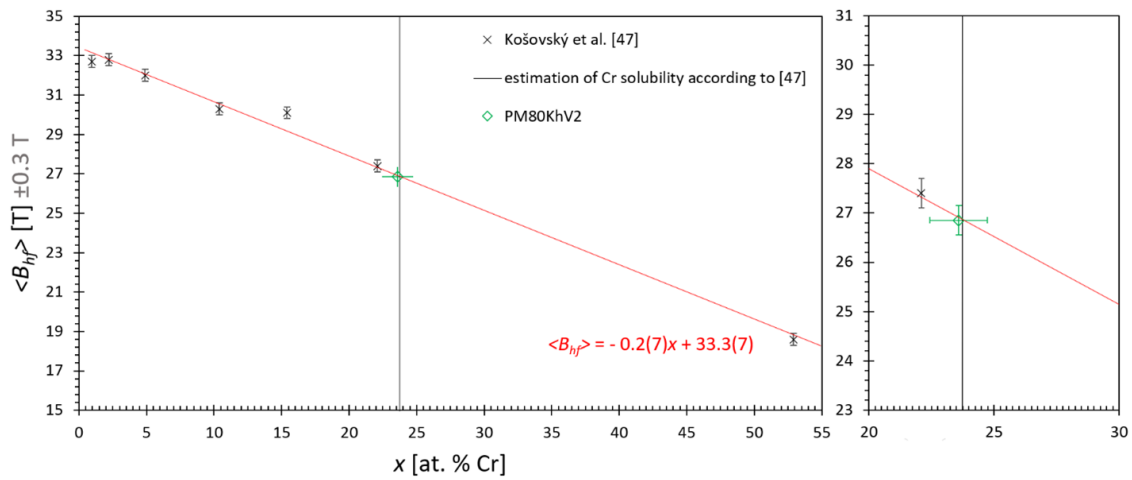
Figure 5. Dependence of the average hyperfine magnetic field, as a function of chromium concentration in Fe-Cr binary alloys.

energy for crystallisation and other model parameters are independent of time and temperature. Under these circumstances, the crystallisation process can be described with the JMAK equation [60–62]:

$$\langle B_{hf}(t) \rangle = \langle B_0 \rangle + \alpha[1 - e^{(1-(kt)^n)}], \qquad (1)$$

where

$\langle B_0 \rangle$ is the average magnetic hyperfine field for the non-annealed steel sample,

k is the rate constant,

n is the Avrami exponent,

α is a free parameter.

The kinetic parameter gives information on the decomposition mechanism and the rate constant can be used for determining the activation energy via the Arrhenius law. The obtained value of the Avrami exponent, n, is equal to 0.52(9), indicating thereby that the process responsible for the phase decomposition in the material could be a diffusion-controlled thickening of plates. The entire recrystallisation process took place in two phases, where the second part of the process at higher annealing times is associated with the

formation of σ-phase. The process of formation of the σ-phase is slow, and therefore, longer annealing times of up to 8000 hours would be necessary for a clearer identification.

The maximum value of Bhft can be used to estimate the solubility limit of chromium in steels at 475 °C. Annealing of steel, however, takes place partially in a linear heating mode. Efficient methods have been proposed for the calculation of kinetic parameters for a non-isothermal measurement. Kissinger's method was used to determine the activation energies of the first and the second stages of crystallisation [59]. On the basis of previous studies [47–49], it can be concluded that the dependence of the magnetic hyperfine field as a function of the impurity atom has a linear character:

$$x \, [\text{at} \, \% \, \text{Cr}] = \frac{\langle B_{hf}(t) \rangle - \langle B_0 \rangle}{\beta}, \qquad (2)$$

where β coefficient describes the decrease of the hyperfine magnetic field with increasing chromium concentration in 1NN-2NN (Figure 5). Based on the results from the articles by Košovský et al. [47] and
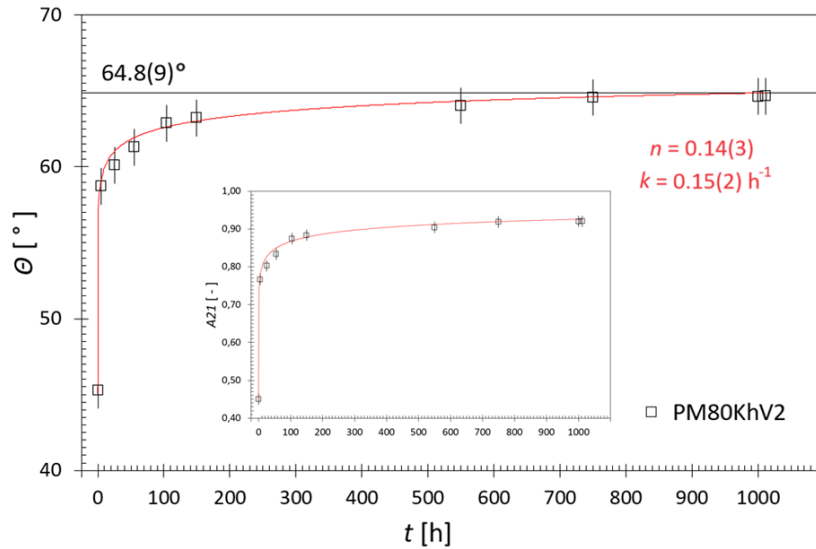
FIGURE 6. Dependence of Θ-angle (and A21) as a function of annealing time. Red solid lines represent the best-fit of the experimental data fitted using Avrami mechanism (Equation (4)).

Dubiel et al. [48, 49, 54], the chromium concentration was calculated, which reaches between 22.4(4) and 24.7(4) at % Cr and is similar to the value determined by the chemical analysis.

The TMS technique provides information about the magnetic arrangement of nanostructures (grains) or of the overall magnetic texture. Specifically, the angle between the local magnetisation vector and the normal vector to the sample surface (the direction of gamma rays). The Θ-angle can be determined from the value of A21 (Equation (3)), which was the fitted parameter:

$$\Theta \ [°] = \arccos\left(\left(\frac{2}{3}A21^{-1} - \frac{1}{2}\right)^{\frac{1}{2}}\right). \qquad (3)$$

The value of A21 varies according to the annealing time, while the saturation course is also assumed (Equation (4)). The dependence of $\Theta(t)$-angle on the annealing time can be seen in Figure 6. It can be noticed that $\Theta(t)$-angle increases with annealing time, i.e. the magnetisation vector rotates towards the sample's surface, however, as evidenced by the inset, the rate of the increase is not constant but tends to saturate within the first ∼1000 hours of annealing. This effect seems to be related to the decomposition and creation of Fe-rich and Cr-rich phase (first stage of the transformation). It is assumed that for longer annealing times, $\Theta(t)$-angle (and A21) continues to increase and saturation of $\Theta(t)$-angle (according to Equation (4)) is obviously related to the growth of grains in the direction parallel to the sample's surface:

$$\langle\Theta(t)\rangle = \langle\Theta_0\rangle + \chi[1 - e^{(1 - (kt)^n)}], \qquad (4)$$

where

$\langle\Theta_0\rangle$ is the angle between the local magnetisation vector and the normal vector to the sample surface

for non-annealed PM80KhV2 steel sample ($\langle\Theta_0\rangle = 45.30°$),

k is the rate constant ($k = 0.15(2)\,\text{h}^{-1}$),

n is the Avrami kinetic exponent ($n = 0.14(3)$),

χ is a free parameter ($\chi = 21.9(8)$).

For longer annealing times (over 5000 hours), a decrease in $\Theta(t)$-angle is assumed, which is associated with σ-phase creation.

The single-line component in the central part of the TMS spectra (Figure 2) may correspond to the structure, where chromium probably segregates to form the paramagnetic Cr-rich phase or locally non-magnetic cementite. Based on the isomer shift of paramagnetic component for the longest annealing time (1012 hours), the solubility limit in α' phase can be estimated (Figure 7). Using the article by Dubiel et al. [54, 62], the calculated solubility limit is 87.1(3) at % at a temperature of 475 °C.

The spectral area of this paramagnetic component increases with the annealing time (Figure 8). This modelled spectral component is in agreement with theoretical calculations where a non-zero probability of the majority presence of chromium atoms around the resonance atom exists, where prevalent number of chromium atoms are supressing the magnetic ordering of resonant nuclei in this chromium rich α' phase, while non-magnetic cementite (Fe_3C) can contribute to this phase as well, if present.

The above interpretation of the paramagnetic component cannot be made with complete certainty due to the low concentration of iron nuclei present in this Cr-rich phase, resulting in a low manifestation of this phase in the TMS spectra. Rising relative area of this paramagnetic component during the prolonged annealing time has a similar course as in the study by Degmová et al. [40], where the authors assigned this
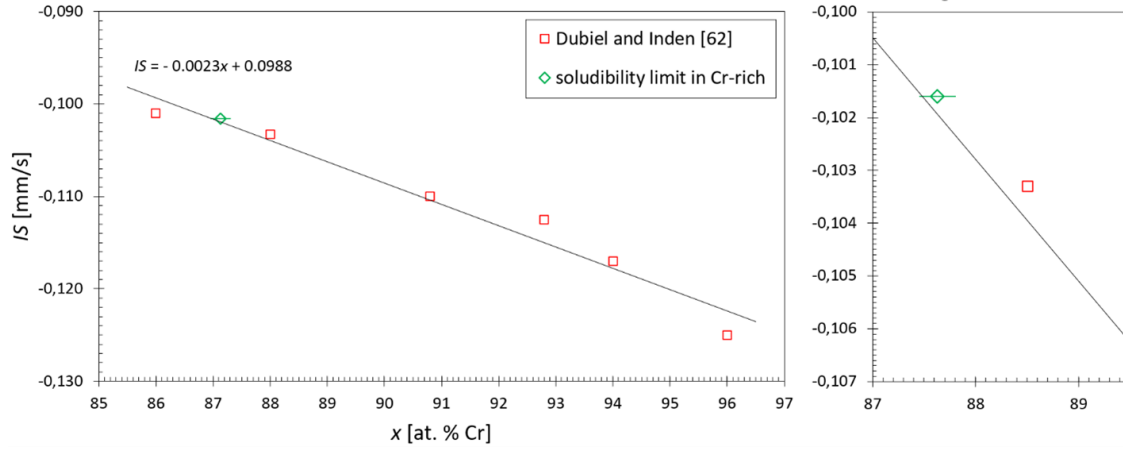
FIGURE 7. Dependence of isomer shift of single-line component as a function of chromium concentration.
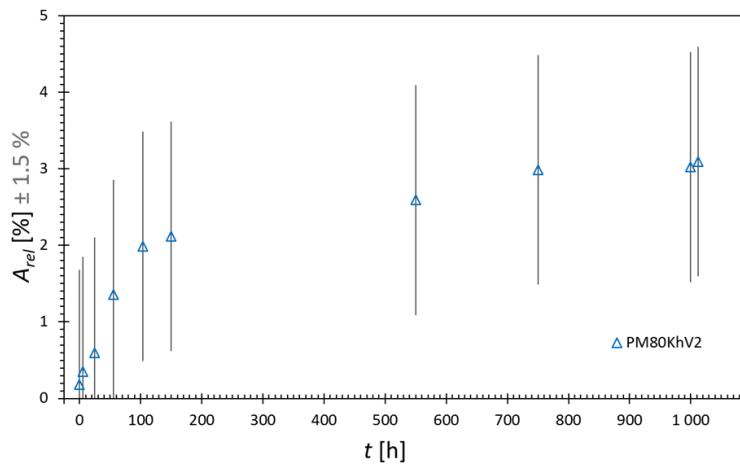

FIGURE 8. Dependence of the relative area of paramagnetic component versus annealing time for the PM80KhV2 ODS steel sample annealed at a temperature of 475 °C, measured by TMS.

paramagnetic phase to the chromium-rich α' phase as well.

3.3. ATOM PROBE TOMOGRAPHY

From the results of Mössbauer spectrometry measurements, it is possible to declare a homogeneous bcc distribution in the materials, and thus one can consider a random distribution of atoms in the sample. One randomly selected Cr-rich nanoprecipitate obtained from a PM80KhV2 steel sample annealed for 1012 hours is shown in Figure 9. The measured chromium concentration in the sample was 21.9 at %. The measurement uncertainty can be determined according to the relationship:

$$\sigma \ [\%] = \frac{x(100 - x)}{\sqrt{\nu}}, \tag{5}$$

where

x is the atomic concentration of chromium,

ν is the number of collected atoms.

Based on the measurements of the unannealed sample, it is possible to say that the distribution of chromium in the sample corresponds to a value of 0.98(1) % with

respect to the distribution determined based on the theoretical binomial distribution model (BDM). No precipitates were observed in the sample where the chromium concentration exceeded the threshold level. These statements are also confirmed by Figure 10, which compares the dependence of the probability of the occurrence of a chromium atom in 1-2NN as a function of the atomic concentration of chromium in the sample, which always represents 100 randomly selected atoms. The theoretical probability was calculated according to the equation:

$$P(m, n) = \frac{M!N!}{\langle m \rangle! \langle n \rangle! (M - \langle m \rangle)! (N - \langle n \rangle)!}$$
$$\times x^{(m+n)} (1 - x)^{((M+N) - m + n)}, \tag{6}$$

where

m is the number of chromium atoms in 1NN,

n is the number of chromium atoms in 2NN,

M is the maximum number of atoms in 1NN (in our case $M = 8$),

N is the maximum number of atoms in 2NN ($N = 6$).

(A). TEM image of APT sample of PM80KhV2 ODS steel annealed at 475 °C for 1012 hours.

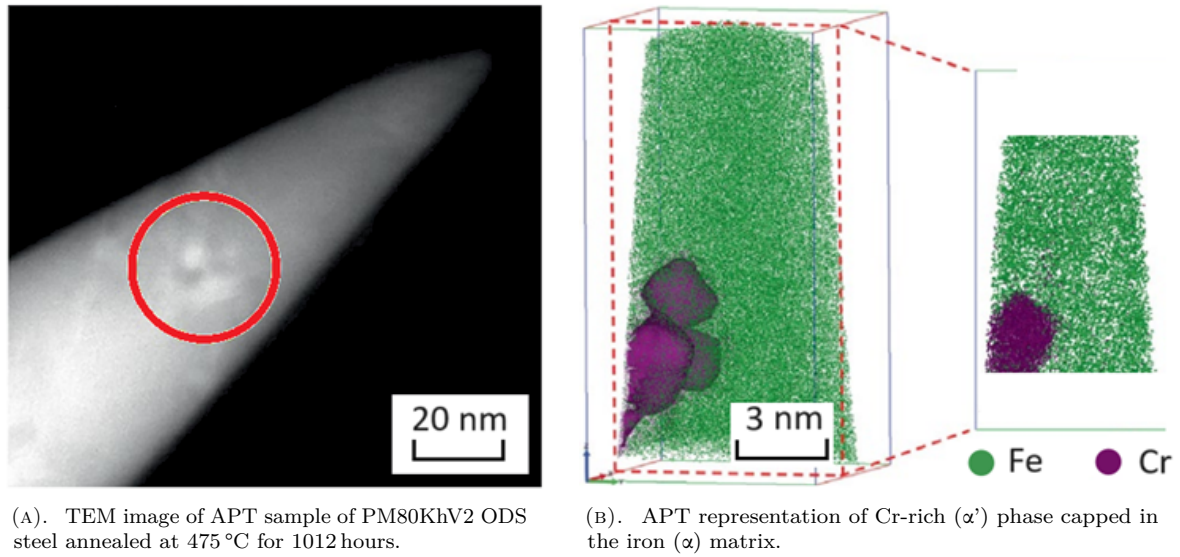(B). APT representation of Cr-rich (α') phase capped in the iron (α) matrix.

FIGURE 9. TEM image of APT sample of PM80KhV2 ODS steel annealed at 475 °C for 1012 hours and APT representation of Cr-rich (α') phase capped in the iron (α) matrix.
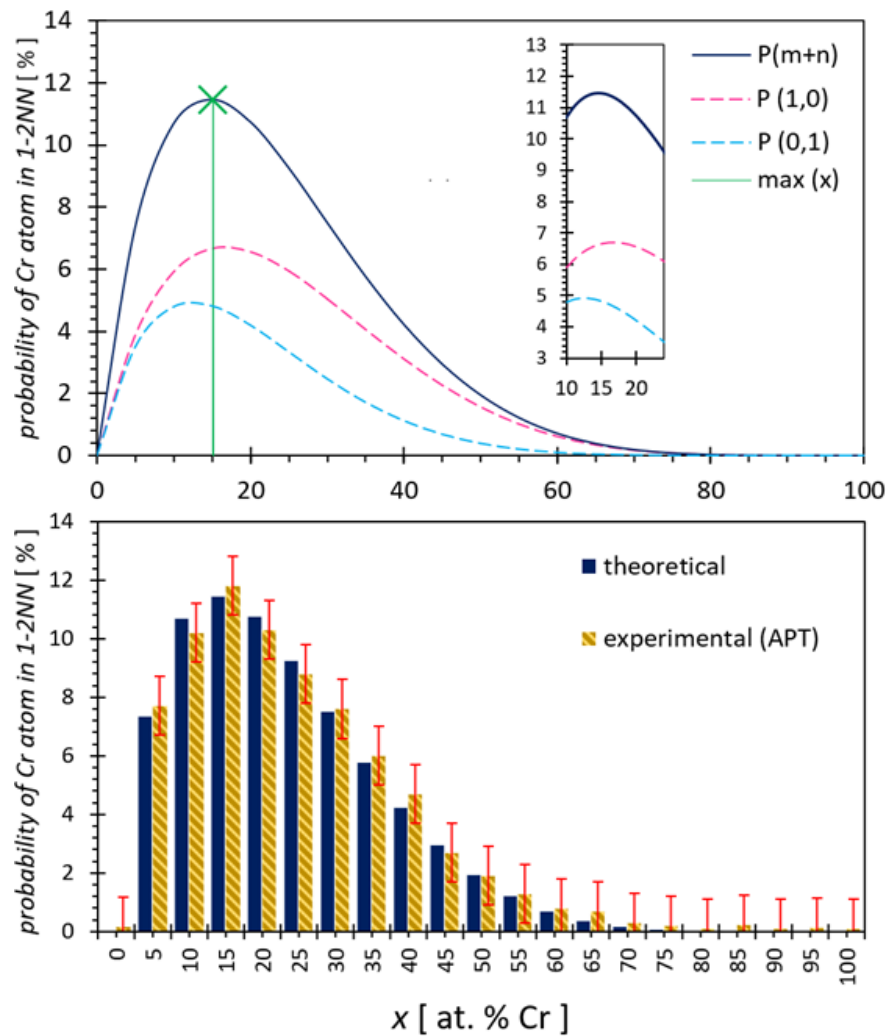

FIGURE 10. Chromium concentration frequency distribution versus concentration of chromium atoms in 1NN-2NN assuming random distribution of atoms. The experimental values are obtained with sampling boxes of 500 atoms.
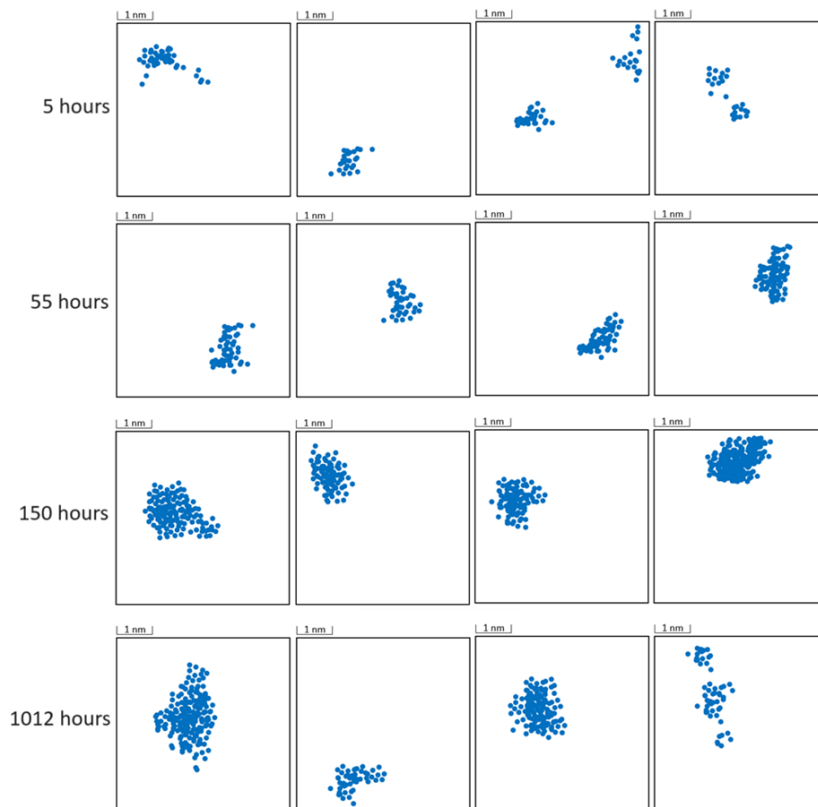
FIGURE 11. Distribution of chromium-enriched precipitates in PM80KhV2 ODS steel after annealing at 475 °C for 5, 55, 150, and 1012 hours. In all images, the data were treated: only Cr-rich region where the local chromium concentration is as high as 60 at % are displayed.

Based on the probability calculations according to Equation (6), it appears that only iron atoms occur in the 1NN-2NN vicinity of the iron probe atom. The probability that there is no chromium atom or one chromium atom in 1NN-2NN reaches the value of 96.9(7) % and therefore it can be approximated that there is a maximum of one impurity atom in each 1NN-2NN structure. On the other hand, the probability that there are 2 or more chromium atoms in the 1NN-2NN neighbourhood reaches 3.0(3) %, and therefore, these configurations can be neglected. The experimental values of the probabilities were calculated with a step of 0.5 at %.

Figure 11 shows the 3D distributions of precipitates consisting of the Cr-rich phase for different annealing times, where the local chromium concentration exceeds 60 at % Cr. There is a segregation of α and α' phases, which is clearly visible from Figure 11. The number of precipitates in the sample is very low (due to the relatively low atomic concentration of chromium), and therefore, precipitates from different parts of the sample volume are shown. The characteristic diameter of the precipitates was calculated based on the averaging of at least 50–260 nanostructures. It can be seen from Figure 11 that the nanostructures have an elliptical character, due to the partial evaporation of the phases in the radial direction. Approximation of near elliptical nanoprecipitates using calculated spherical structures actually introduces an

error of less than 0.4 %, which is less than the resolving power of the APT technique. The radius of each nanostructure is derived from the number of detected atoms in the precipitate and is given as follows:

$$\rho = \left(\frac{3\nu a^3}{8\pi Q} \right)^{\frac{1}{2}}, \qquad (7)$$

where

ν is the number of atoms detected by APTin the nanoprecipitate,

Q is the atom probe detector efficiency ($Q = 0.5$),

a is the lattice parameter.

From Figure 11, it can be concluded that in the case of high-chromium steels, the formation of precipitates takes place in different local materials and with increasing time, they are connected through the so-called neck.

The initial nuclei of the precipitates are oriented randomly, and it is not possible to establish a preferential direction of their growth. As the annealing time increases (over 55 hours), the nanoprecipitates increase, and this statement about the formation of precipitates is also confirmed by the values of the Avrami kinetic parameter from the JMAK mechanism. The mechanism of precipitation formation is consistent with other types of steel and with theoretical binary alloys. The concentration of chromium in the
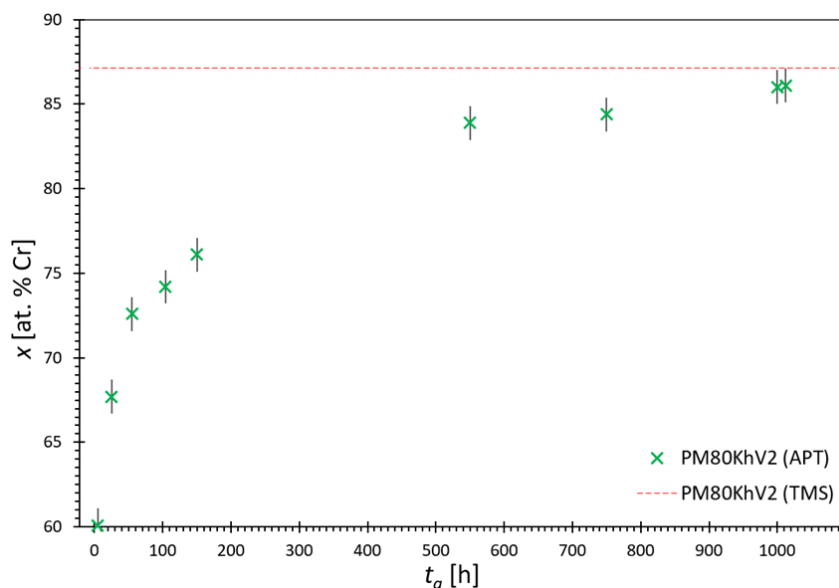
FIGURE 12. Temporal evolution of the chromium concentration of the α' phase in PM80KhV2 at 475 °C. Dashed line represents solubility limit of chromium in α' precipitates determined by TMS.
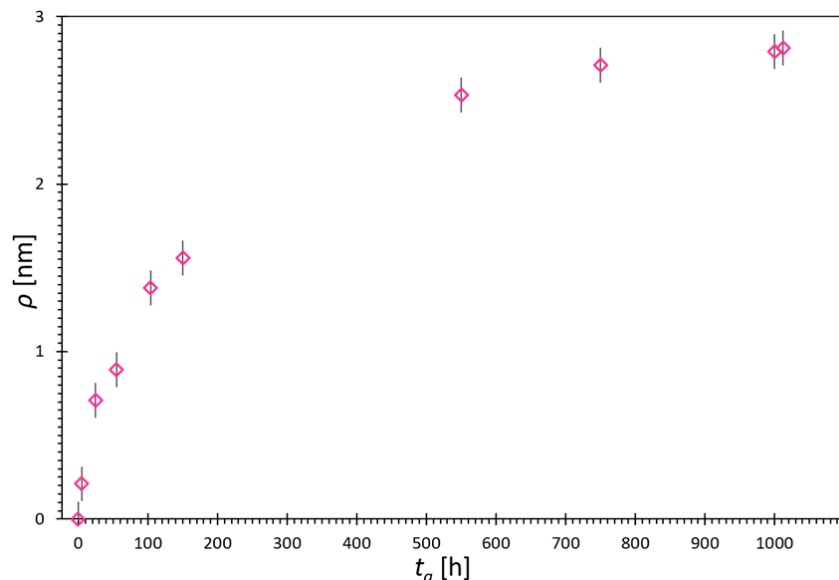

FIGURE 13. Annealing time dependence of the average precipitate radius in PM80KhV2 high-chromium ODS steel.

α' precipitates increases with time (Figure 12), with a maximum value that is assumed to saturate to that determined by TMS. However, this statement cannot be said with certainty, since due to the low concentration, much longer annealing times would be required. These conclusions are in agreement with the work by Dubiel et al., who annealed the samples for more than 4 years. The dependence of the characteristic diameter of Cr-rich precipitates (calculated using Equation (7)) as a function of annealing time is shown in Figure 13. Figure 14 shows the chromium dependence of randomly selected 20 precipitates as a function of precipitate radius during 5, 150 and 1012 hours of annealing at 475 °C. It can be concluded that for the given average size of the α' precipitates, a correlation with the concentration of chromium atoms in the

precipitates cannot be clearly determined. The size and enrichment of the precipitates with chromium is clearly dependent only on the annealing time.

4. CONCLUSION

We demonstrated the applicability of statistical (Gaussian) distribution model used for high-chromium steels and also high-chromium binary Fe-Cr alloys. The Gaussian distribution model of magnetic components is presented, where the residual paramagnetic phase is modelled by one singlet that corresponds to the paramagnetic structure rich in chromium at RT. The sample was subjected to prolonged annealing at a temperature of 475 °C from 5 up to 1012 hours and subsequent structural changes were observed by TMS and APT techniques. The applied fitting model for the TMS
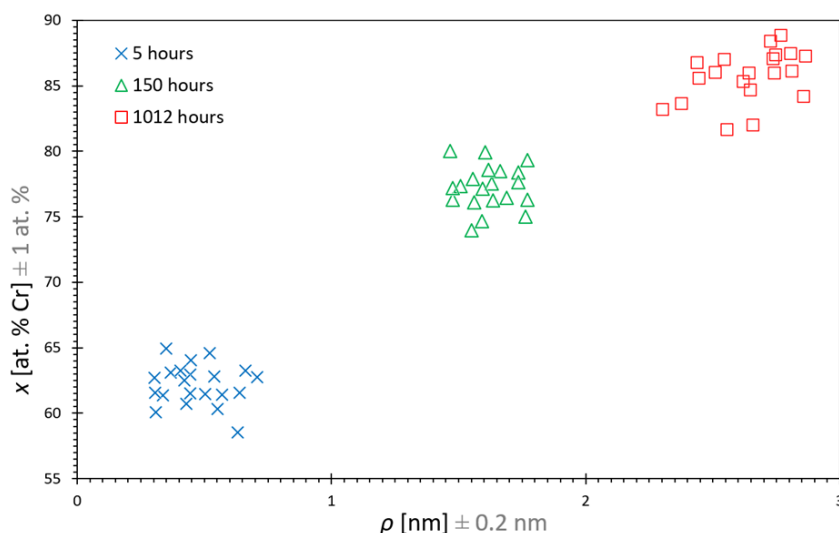
FIGURE 14. Chromium concentration in α' precipitates as a function of their radii for 5, 150, and 1012 hours of ageing in a PM80KhV2 steel at 475 °C.

spectra evaluation using the distribution has proven to be suitable tool for the interpretation of the structural changes occurring in the materials as a result of its long-term annealing at a constant temperature of 475 °C. With increasing annealing time, the magnetic hyperfine field values of the sextets saturate at 26.8(5) T, from which the solubility limit of chromium in the Fe-rich phase can be estimated. The solubility limit was determined to be $23.5(9) \pm 0.5(0)$ at % Cr. Within the experimental error, the calculated value is identical to the value obtained from the chemical analyses. In the middle of the spectra, a single-line component is observed, which can be interpreted as a chromium rich (α') phase or as another non-magnetic phase (like nanosized, superparamagnetic, cementite). It represents a minor fraction of iron nuclei in the spectral areas in all analysed spectra and can be associated with the onset of Cr-rich clusters formation. Based on the isomer shift of the singlet, the solubility limit in α' (Cr-rich) phase was estimated at 87.1(3) at %. Using the APT technique, it was possible to describe the 3D structure of α' precipitates after individual annealing steps. This method made it possible to describe, in detail, the time development of the formation of the Cr-rich phase, whereby it was possible to observe the saturation trend. Based on the development of the size of the precipitates and the relative representation of chromium in the precipitates, a clear correlation between these two quantities cannot be established. Using APT, it is possible to monitor and also predict microstructural changes that have a fundamental impact on changes in macroscopic properties.

REFERENCES

[1] J.-O. Nilsson. Super duplex stainless steels. *Materials Science and Technology* **8**(8):685–700, 1992. https://doi.org/10.1179/mst.1992.8.8.685

[2] D. Košovský, J. Dekan, K. Sedlačková, M. Miglierini. Microstructure of high-chromium ferritic-martensitic steels for next-generation reactors. *Physica Status Solidi (B)* **261**(3):2300526, 2023. https://doi.org/10.1002/pssb.202300526

[3] T. Kim, S. Noh, S. Kang, et al. Development of advanced radiation resistant ODS steel for fast reactor system applications. *World Journal of Engineering and Technology* **3**(3C):125–128, 2015. https://doi.org/10.4236/wjet.2015.33C019

[4] Z. Oksiuta, P. Olier, Y. de Carlan, N. Baluc. Development and characterisation of a new ODS ferritic steel for fusion reactor application. *Journal of Nuclear Materials* **393**(1):114–119, 2009. https://doi.org/10.1016/j.jnucmat.2009.05.013

[5] G. Sundararajan, R. Vijay, A. V. Reddy. Development of 9Cr ferritic-martensitic and 18Cr ferritic oxide dispersion strengthened steels. *Current Science* **105**(8):1100–1106, 2013.

[6] R. L. Klueh, J. P. Shingledecker, R. W. Swindeman, D. Hoelzer. Oxide dispersion-strengthened steels: A comparison of some commercial and experimental alloys. *Journal of Nuclear Materials* **341**(2):103–114, 2005. https://doi.org/10.1016/j.jnucmat.2005.01.017

[7] M. S. El-Genk, J.-M. Tournier. A review of refractory metal alloys and mechanically alloyed-oxide dispersion strengthened steels for space nuclear power systems. *Journal of Nuclear Materials* **340**(1):93–112, 2005. https://doi.org/10.1016/j.jnucmat.2004.10.118

[8] K. Murty, I. Charit. Structural materials for Gen-IV nuclear reactors: Challenges and opportunities. *Journal of Nuclear Materials* **383**(1):189–195, 2008. https://doi.org/10.1016/j.jnucmat.2008.08.044

[9] E. Lucon, A. Leenaers, W. Vandermeulen. Mechanical response of oxide dispersion strengthened (ODS) EUROFER97 after neutron irradiation at 300 °C. *Fusion Engineering and Design* **82**(15):2438–2443, 2007. https://doi.org/10.1016/j.fusengdes.2007.05.018

[10] S. Ahila, B. Reynders, H. J. Grabke. The evaluation of the repassivation tendency of Cr-Mn and Cr-Ni steels using scratch technique. *Corrosion Science* **38**(11):1991–2005, 1996. https://doi.org/10.1016/S0010-938X(96)00092-3

[11] J. W. Park, V. S. Rao, H. S. Kwon. Effects of nitrogen on the repassivation behavior of type 304L stainless steel in chloride solution. *Corrosion* **60**(12):1099–1103, 2004. https://doi.org/10.5006/1.3299223

[12] R. Sizmann. The effect of radiation upon diffusion in metals. *Journal of Nuclear Materials* **69–70**:386–412, 1978. https://doi.org/10.1016/0022-3115(78)90256-8

[13] C. Cabet, F. Dalle, E. Gaganidze, et al. Ferritic-martensitic steels for fission and fusion applications. *Journal of Nuclear Materials* **523**:510–537, 2019. https://doi.org/10.1016/j.jnucmat.2019.05.058

[14] L. Tan, Y. Katoh, A.-A. Tavassoli, et al. Recent status and improvement of reduced-activation ferritic-martensitic steels for high-temperature service. *Journal of Nuclear Materials* **479**:515–523, 2016. https://doi.org/10.1016/j.jnucmat.2016.07.054

[15] F. Garner, M. Toloczko, B. Sencer. Comparison of swelling and irradiation creep behavior of fcc-austenitic and bcc-ferritic/martensitic alloys at high neutron exposure. *Journal of Nuclear Materials* **276**(1–3):123–142, 2000. https://doi.org/10.1016/S0022-3115(99)00225-1

[16] M. B. Miglierini, L. Pašteka, M. Cesnek, et al. Influence of surface treatment on microstructure of stainless steels studied by Mössbauer spectrometry. *Journal of Radioanalytical and Nuclear Chemistry* **322**(3):1495–1503, 2019. https://doi.org/10.1007/s10967-019-06737-w

[17] V. Slugen, J. S. Veternikova, J. Degmova, et al. Positron annihilation studies of Eurofer97/ODS steels after helium ion implantation. *Nuclear Materials and Energy* **34**:101369, 2023. https://doi.org/10.1016/j.nme.2023.101369

[18] P. Grgac, R. Moravcik, M. Kusy, et al. Thermal stability of metastable austenite in rapidly solidified chromium-molybdenum-vanadium tool steel powder. *Materials Science and Engineering: A* **375–377**:581–584, 2004. https://doi.org/10.1016/j.msea.2003.10.036

[19] M. Kusy, P. Grgac, M. Behulova, et al. Morphological variants of carbides of solidification origin in the rapidly solidified powder particles of hypereutectic iron alloy. *Materials Science and Engineering: A* **375–377**:599–603, 2004. https://doi.org/10.1016/j.msea.2003.10.095

[20] M. Miglierini. Austenite-to-martenzite transformations in ledebourite-type powder steels. *Czechoslovak Journal of Physics* **55**(7):813–822, 2005. https://doi.org/10.1007/s10582-005-0083-1

[21] M. Miglierini, A. Lančok, M. Kusý. Characterization of rapidly solidified powder of high-speed steel. *Hyperfine Interactions* **190**(1):51–57, 2009. https://doi.org/10.1007/s10751-009-9921-z

[22] A. Lančok, T. Kmječ, M. Štefánik, et al. Structural characterization of highly corrosion-resistant steel. *Croatica Chemica Acta* **88**(4):355–361, 2016. https://doi.org/10.5562/cca2794

[23] F. A. Garner, M. B. Toloczko, B. H. Sencer. Comparison of swelling and irradiation creep behavior of fcc-austenitic and bcc-ferritic/martensitic alloys at high neutron exposure. *Journal of Nuclear Materials* **276**(1):123–142, 2000. https://doi.org/10.1016/S0022-3115(99)00225-1

[24] A. Kohyama, A. Hishinuma, D. S. Gelles, et al. Low-activation ferritic and martensitic steels for fusion application. *Journal of Nuclear Materials* **233–237**:138–147, 1996. https://doi.org/10.1016/S0022-3115(96)00327-3

[25] D. McClintock, M. Sokolov, D. Hoelzer, R. Nanstad. Mechanical properties of irradiated ODS-EUROFER and nanocluster strengthened 14YWT. *Journal of Nuclear Materials* **392**(2):353–359, 2009. Nuclear Fuels and Structural Materials 2. https://doi.org/10.1016/j.jnucmat.2009.03.024

[26] L. Tan, Y. Katoh, L. Snead. Development of castable nanostructured alloys as a new generation RAFM steels. *Journal of Nuclear Materials* **511**:598–604, 2018. https://doi.org/10.1016/j.jnucmat.2018.05.024

[27] E. Lucon, R. Chaouadi, M. Decréton. Mechanical properties of the european reference RAFM steel (EUROFER97) before and after irradiation at 300 °C. *Journal of Nuclear Materials* **329–333**:1078–1082, 2004. https://doi.org/10.1016/j.jnucmat.2004.04.023

[28] T. Yamamoto, G. R. Odette, H. Kishimoto, et al. On the effects of irradiation and helium on the yield stress changes and hardening and non-hardening embrittlement of ∼8Cr tempered martensitic steels: Compilation and analysis of existing data. *Journal of Nuclear Materials* **356**(1):27–49, 2006. https://doi.org/10.1016/j.jnucmat.2006.05.041

[29] E. Gaganidze, C. Petersen, E. Materna-Morris, et al. Mechanical properties and TEM examination of RAFM steels irradiated up to 70dpa in BOR-60. *Journal of Nuclear Materials* **417**(1):93–98, 2011. https://doi.org/10.1016/j.jnucmat.2010.12.047

[30] V. Kuksenko, C. Pareige, C. Genevois, P. Pareige. Characterisation of Cr, Si and P distribution at dislocations and grain-boundaries in neutron irradiated Fe-Cr model alloys of low purity. *Journal of Nuclear Materials* **434**(1):49–55, 2013. https://doi.org/10.1016/j.jnucmat.2012.11.027

[31] M. McLean. On the threshold stress for dislocation creep in particle strengthened alloys. *Acta Metallurgica* **33**(4):545–556, 1985. https://doi.org/10.1016/0001-6160(85)90018-5

[32] N. Wang, Y. Ji, Y. Wang, et al. Two modes of grain boundary pinning by coherent precipitates. *Acta Materialia* **135**:226–232, 2017. https://doi.org/10.1016/j.actamat.2017.06.031

[33] E. Arzt, D. Wilkinson. Threshold stresses for dislocation climb over hard particles: The effect of an attractive interaction. *Acta Metallurgica* **34**(10):1893–1898, 1986. https://doi.org/10.1016/0001-6160(86)90247-6

[34] B. Reppich. On the attractive particle-dislocation interaction in dispersion-strengthened material. *Acta Materialia* **46**(1):61–67, 1998. https://doi.org/10.1016/S1359-6454(97)00234-6

[35] A. Chauhan, D. Litvinov, Y. de Carlan, J. Aktaa. Study of the deformation and damage mechanisms of a 9Cr-ODS steel: Microstructure evolution and fracture characteristics. *Materials Science and Engineering: A* **658**:123–134, 2016. https://doi.org/10.1016/j.msea.2016.01.109

[36] J. Schröder, E. Arzt. Weak beam studies of dislocation/dispersoid interaction in an ODS superalloy. *Scripta Metallurgica* **19**(9):1129–1134, 1985. https://doi.org/10.1016/0036-9748(85)90022-5

[37] B. Ravelo, F. Vurpillot. Analysis of excitation pulsed signal propagation for atom probe tomography system. *Progress In Electromagnetics Research Letters* **47**:61–70, 2014. https://doi.org/10.2528/PIERL14042403

[38] Z. Foxman, O. Sobol, M. Pinkas, et al. Microstructural evolution of Cr-rich ODS steels as a function of heat treatment at 475 °C. *Metallography, Microstructure, and Analysis* **1**(3):158–164, 2012. https://doi.org/10.1007/s13632-012-0028-6

[39] Z. Száraz, G. Török, V. Kršjak, P. Hähner. SANS investigation of microstructure evolution in high chromium ODS steels after thermal ageing. *Journal of Nuclear Materials* **435**(1–3):56–62, 2013. https://doi.org/10.1016/j.jnucmat.2012.12.016

[40] J. Degmová, V. Kršjak, S. Sojak, et al. NDT study of precipitation processes in thermally aged Fe-20Cr alloy. *Journal of Nuclear Materials* **547**:152799, 2021. https://doi.org/10.1016/j.jnucmat.2021.152799

[41] D. Košovský, M. Miglierini, M. Pavúk, T. Kmječ. Surface features of binary $Fe_{100-x}Cr_x$ ($1 \leq x \leq 50$) alloys. *AIP Conference Proceedings* **2778**(1):030006, 2023. https://doi.org/10.1063/5.0136328

[42] S. M. Dubiel, J. Żukrowski. Kinetics of transformation, border of metastable miscibility gap in Fe-Cr alloy and limit of Cr solubility in iron at 858 K. *Metallurgical and Materials Transactions A* **54**(8):3240–3248, 2023. https://doi.org/10.1007/s11661-023-07092-y

[43] F. De Geuser, B. Gault. Metrology of small particles and solute clusters by atom probe tomography. *Acta Materialia* **188**:406–415, 2020. https://doi.org/10.1016/j.actamat.2020.02.023

[44] E. W. Müller, K. Bahadur. Field ionization of gases at a metal surface and the resolution of the field ion microscope. *Physical Review* **102**:624–631, 1956. https://doi.org/10.1103/PhysRev.102.624

[45] T. F. Kelly, M. K. Miller. Atom probe tomography. *Review of Scientific Instruments* **78**(3):031101, 2007. https://doi.org/10.1063/1.2709758

[46] T. Žák, Y. Jirásková. CONFIT: Mössbauer spectra fitting program. *Surface and Interface Analysis* **38**(4):710–714, 2006. https://doi.org/10.1002/sia.2285

[47] D. Košovský, M. Miglierini, M. Pavúk, et al. Mössbauer spectrometry of model binary $Fe_{100-x}Cr_x$ ($1 \leq x \leq 50$) alloys. *Physica Status Solidi (B)* **259**(6):2100632, 2022. https://doi.org/10.1002/pssb.202100632

[48] S. M. Dubiel, J. Zukrowski. Mössbauer effect study of charge and spin transfer in Fe-Cr. *Journal of Magnetism and Magnetic Materials* **23**(2):214–228, 1981. https://doi.org/10.1016/0304-8853(81)90137-2

[49] S. Dubiel, J. Żukrowski. Phase-decomposition-related short-range ordering in an Fe-Cr alloy. *Acta Materialia* **61**(16):6207–6212, 2013. https://doi.org/10.1016/j.actamat.2013.07.003

[50] R. Idczak, K. Idczak, R. Konieczny. $Fe_{0.88}Cr_{0.12}$ and $Fe_{0.85}Cr_{0.15}$ alloys exposed to air at 870 K studied by TMS, CEMS and XPS. *Physica B: Condensed Matter* **528**:27–36, 2018. https://doi.org/10.1016/j.physb.2017.10.082

[51] R. Idczak, K. Idczak, R. Konieczny. Oxidation and surface segregation of chromium in Fe-Cr alloys studied by Mössbauer and X-ray photoelectron spectroscopy. *Journal of Nuclear Materials* **452**(1):141–146, 2014. https://doi.org/10.1016/j.jnucmat.2014.05.003

[52] R. Idczak, R. Konieczny, J. Chojcan. Atomic short-range order in $Fe_{1-x}Cr_x$ alloys studied by ^{57}Fe Mössbauer spectroscopy. *Journal of Physics and Chemistry of Solids* **73**(9):1095–1098, 2012. https://doi.org/10.1016/j.jpcs.2012.05.010

[53] R. Konieczny, R. Idczak, J. Chojcan. Mössbauer studies of interactions between titanium atoms dissolved in iron. *Hyperfine Interactions* **219**(1):121–127, 2013. https://doi.org/10.1007/s10751-012-0653-0

[54] S. M. Dubiel, G. Inden. On the miscibility gap in the Fe-Cr system: A Mößbauer study on long term annealed alloys. *International Journal of Materials Research* **78**(8):544–549, 1987. https://doi.org/doi:10.1515/ijmr-1987-780802

[55] S. M. Dubiel, J. Cieslak. Short-range order in iron-rich Fe-Cr alloys as revealed by Mössbauer spectroscopy. *Physical Review B* **83**:180202(R), 2011. https://doi.org/10.1103/PhysRevB.83.180202

[56] S. M. Dubiel, J. Cieślak, H. Reuther. Effect of He^+ irradiation on Fe-Cr alloys: Mössbauer-effect study. *Journal of Nuclear Materials* **434**(1):235–239, 2013. Special Section on Spent Nuclear Fuel. https://doi.org/10.1016/j.jnucmat.2012.10.048

[57] S. M. Dubiel, J. Żukrowski. Change of Cr atoms distribution in $Fe_{85}Cr_{15}$ alloy caused by 250keV He^+ ion irradiation to different doses. *Journal of Alloys and Compounds* **624**:165–169, 2015. https://doi.org/10.1016/j.jallcom.2014.11.070

[58] R. Idczak, R. Konieczny, J. Chojcan. Atomic short-range order in $Fe_{1-x}Cr_x$ alloys studied by ^{57}Fe Mössbauer spectroscopy. *Journal of Physics and Chemistry of Solids* **73**(9):1095–1098, 2012. `https://doi.org/10.1016/j.jpcs.2012.05.010`

[59] H. E. Kissinger. Reaction kinetics in differential thermal analysis. *Analytical Chemistry* **29**(11):1702–1706, 1957. `https://doi.org/10.1021/ac60131a045`

[60] S. M. Dubiel, J. Żukrowski. On the miscibility gap at 800 K in the Fe-Cr alloy system. *Materials Research Express* **6**(2):026568, 2018. `https://doi.org/10.1088/2053-1591/aaf18d`

[61] S. M. Dubiel. Microscopic reasons for brittleness of high-chromium steels. *Hyperfine Interactions* **111**(1):211–214, 1998. `https://doi.org/10.1023/A:1012609918629`

[62] S. M. Dubiel. What can one learn about Fe-Cr alloys using Mössbauer spectroscopy? *Critical Reviews in Solid State and Materials Sciences* pp. 1–52, 2023. `https://doi.org/10.1080/10408436.2023.2273462`